



Single-step conversion of ethanol into n-butene-rich olefins over metal catalysts supported on ZrO₂-SiO₂ mixed oxides

Vanessa Lebarbier Dagle^{a,*}, Gregory Collinge^a, Mohammed Rahman^a, Austin Winkelman^{a,b}, Wenda Hu^a, Jian Zhi Hu^{a,b}, Libor Kovarik^a, Mark Engelhard^a, Jennifer Jocz^a, Yong Wang^{a,b}, Mal-Soon Lee^a, Vassiliki-Alexandra Glezakou^{a,1}, Debmalya Ray^a, Roger Rousseau^{a,*}, Robert Dagle^{a,*}

^a Pacific Northwest National Laboratory, 902 Battelle Blvd., Richland, WA 99354, USA

^b Voiland School of Chemical Engineering and Bioengineering, Washington State University, Pullman, WA 99164, USA

ARTICLE INFO

Keywords:

Ethanol
N-butene
Olefins
Biomass
Sustainable aviation fuel

ABSTRACT

With airlines committed to drastically reduce their carbon footprint by 2050, producing jet fuel from renewable ethanol is of particular interest. Recently, we reported on an Ag/ZrO₂/SBA-16 catalyst that is very effective for directly converting ethanol into n-butene-rich olefins jet fuel precursors (i.e., 88% at full conversion). Here, we report on a Cu/ZrO₂/SBA-16 catalyst that presents remarkable olefins selectivity (i.e., 89% at 96% conversion) and enhanced stability as compared to Ag/ZrO₂/SBA-16 catalyst. Under severe operating conditions a conversion loss < 10% was observed with the Cu/ZrO₂/SBA-16 catalyst as compared to a 50% loss of conversion with the Ag/ZrO₂/SBA-16 catalyst. Combined experimental and computational tools revealed that replacing Ag with Cu shifts the reaction pathway of crotonaldehyde hydrogenation from 1,3-butadiene (i.e., coke precursor) production to butyraldehyde formation. Experiments conducted with 4%Cu/4%ZrO₂ supported on SBA-16, dealuminated zeolite Beta, and aluminum silicate revealed the performance and stability advantage of the SBA-16-supported catalyst.

1. Introduction

The global consumption of jet fuel is ~106 billion gallon/year which is expected to double by 2050, potentially resulting in a significant increase of global greenhouse gas emissions from the aviation sector [1]. With airlines committing to reduce their carbon footprint by 50% before 2050, sustainable aviation fuel (SAF) production has become a prominent strategy for reducing the CO₂ footprint [2,3], since opportunities for aircraft electrification are very limited in the near-term due to the low energy density of batteries [1,4]. However, current production of SAF represents less than 1% of the global jet fuel demand [5]. Many processes have been investigated to convert biomass into jet fuel [3, 6–8], and commercial production of SAF is emerging. However, new technologies are still needed to increase SAF production to meet the 2050 net zero emissions goals.

Ethanol represents a promising platform molecule for the production of fuels and chemicals from renewable resources. Currently, most

ethanol is produced by fermenting sugars derived from corn starch or sugar cane. Nonedible cellulosic feedstocks are attractive because they are widely available, abundant, and relatively inexpensive; however, they currently represent a more costly option for producing ethanol [9]. Ethanol also can be produced by enzymatic or thermocatalytic upgrading of syngas derived from biomass, municipal solid waste, or industrial waste gases (e.g., from steel mills) [10–15]. Taken together, the ethanol “blend wall” coupled with advancements in production efficiency and feedstock diversification may potentially lead to excess ethanol at competitive prices available for the production of a wide range of fuels and commodity chemicals [16].

The production of distillate fuel from ethanol is commercially done using the alcohol-to-jet technology, which involves multiple processing steps. Ethanol initially undergoes catalytic dehydration to form ethylene which is subsequently oligomerized over solid acid catalyst(s). Olefins are then hydrogenated to form paraffins followed by fractionation into jet-range blendstock. Ethylene oligomerization can proceed in either

* Corresponding authors.

E-mail addresses: vanessa.dagle@pnnl.gov (V.L. Dagle), rousseau@ornl.gov (R. Rousseau), robert.dagle@pnnl.gov (R. Dagle).

¹ Current Address: Chemical Sciences Division, Oak Ridge National Laboratory, Oak Ridge, TN 37830, USA

one or two steps [17–20]. Single-step ethylene oligomerization has low selectivity toward fuel-range hydrocarbons because of the high selectivity to undesirable C₁–C₄ light hydrocarbons (~40%) [21–24]. Thus, a two-step ethylene oligomerization process has been reported in which ethylene is first oligomerized to an n-butene-rich olefin stream and then oligomerized to jet-range olefins [19]. For example, we have reported a two-step oligomerization process that produces primarily isoparaffinic hydrocarbons forming minimal aromatic compounds, facilitates efficient conversion of high carbon fractions to distillate range fuels, and minimizes formation of naphtha-like compounds by efficient intermediate product recycling [19,20].

Recently, we demonstrated that Ag/ZrO₂/SBA-16 catalysts are active for direct conversion of ethanol into butadiene or n-butene [25–27]. Single step conversion of ethanol to n-butene is slightly exothermic. It is attractive compared to the ethanol-derived ethylene two-step oligomerization process [19] because of the elimination of ethanol dehydration to ethylene step that is endothermic. For Ag/ZrO₂/SBA-16 catalysts, we showed that when switching from an inert environment (i.e., N₂) to a reducing environment (i.e., H₂), n-butene is produced instead of 1,3-butadiene [26]. The reducing atmosphere leads to partial hydrogenation of 1,3-butadiene into n-butene as opposed to full hydrogenation to n-butane due to the mild hydrogenation properties of Ag. Given that Cu also presents mild hydrogenation properties, it is a potential candidate for direct conversion of ethanol to n-butene.

2. Experimental and computational methods

In this study, we studied Cu/ZrO₂/SBA-16 catalysts for direct conversion of ethanol to n-butene. Operando ¹H MAS (magic angle spinning) NMR (nuclear magnetic resonance) was used to elucidate the reaction mechanism over 4% Cu/4%ZrO₂/SBA-16 catalyst, and in comparison, with 4%Ag/4%ZrO₂/SBA-16 catalyst. We conducted a computational study to understand pathway bifurcations from crotonaldehyde intermediate in relation with the nature of the metal (Ag vs. Cu). The stability of these catalysts also was examined for about 100 h on stream and the fresh and spent catalysts were characterized using scanning transmission electron microscopy (STEM), total carbon analysis, and N₂ adsorption to explain the deactivation behavior. The effect of the catalyst formulation on the catalytic performance was investigated for Cu loadings between 2 and 16 wt% and for Cu/4%ZrO₂ catalysts supported on SBA-16, dealuminated zeolite Beta, and aluminum silicate. The impact of the H₂/N₂ ratio in the feed on the conversion and selectivity to olefins and butadiene was studied for the 2%Cu/4%ZrO₂/SBA-16 catalyst. Finally, we evaluated the impact of the feedstock composition on the catalyst performance of 4% Cu/4%ZrO₂/SBA-16 with ethanol, acetaldehyde, ethanol + acetaldehyde mixture, and ethanol + crotonaldehyde mixture.

2.1. Catalysts preparation

A series of xCu/4ZrO₂/SBA-16 catalysts were synthesized by incipient wetness impregnation of SiO₂ (SBA-16, ACS Materials) with copper nitrate powder and zirconyl nitrate solution dissolved in deionized water. After impregnation, the catalysts were dried at 110°C for 8 h and calcined at 550°C for 4 h. The copper loading “x” was varied from 2 to 16 wt%. A 4Ag/4ZrO₂/SiO₂ catalyst was prepared according to the same method using silver nitrate powder. A 4Cu/4ZrO₂/dealuminated zeolite and a 4Cu/4ZrO₂/SiO₂-Al₂O₃ also were synthesized according to the same method using a dealuminated zeolite beta (Si/Al >300, Zeolyst) and an aluminum silicate (Karpov chemical plant) support instead of SBA-16.

2.2. Brunauer-Emmett-Teller (BET) surface

Nitrogen adsorption was measured at 77 K with an automatic adsorptiometer (Micromeritics ASAP 2000). Samples were pretreated at

150 °C for 12 h under vacuum. The surface areas were determined from adsorption values for five relative pressures (P/P₀) ranging from 0.05 to 0.2 using the BET surface method.

2.3. NMR

The operando ¹H MAS NMR spectra were collected on a 300 MHz Varian Inova NMR spectrometer operating at a ¹H Larmor frequency of 299.97 MHz. The 4Cu/4ZrO₂/SBA-16 catalyst was thermally treated in a glass tube under flowing Ar at 450 °C for 8 h and then reduced at 400 °C in flowing 10% H₂/He for 1 h. The glass tube then was sealed and moved into a dry, N₂-purged glovebox. The desired quantity of catalysts and liquid were charged into a homemade in situ NMR rotor, and gaseous components were subsequently charged into the rotor with a high-pressure loading chamber [28–30]. Samples sealed in the rotor were spun at the magic angle at a spinning rate of 4000 Hz in a commercial 7.5 mm ceramic probe. A single-pulse with width of 3.5 μs (corresponding to a 90° pulse angle for maximizing the sensitivity), a recycle delay time of 0.5 s, and an acquisition time of 0.17 s were used to collect 128 no. of scans per spectrum. This corresponds to a temporal resolution of 66 s (1.1 min) per spectrum. The 0.5 s recycle delay was selected by carrying out a series of experiments on the catalytic reaction systems under the same condition where the recycle delay was varied from 0.1 to 10 s. The 0.5 s recycle delay is sufficiently long for all the signals to be quantitatively excited. The experimental temperature was controlled using a commercial variable-temperature heating stack, externally calibrated with an ethylene glycol thermometer. The temperature was elevated from 35 °C to 210 °C at a rate of ~14 °C/min during experimental runs.

2.4. X-ray photoelectron spectroscopy (XPS)

XPS measurements were performed with a Physical Electronics Quantera SXM Scanning X-ray Microprobe. This system uses a focused monochromatic Al Kα X-ray (1486.7 eV) source for excitation and a spherical section analyzer. The instrument has a 32-element multi-channel detection system. The X-ray beam is incident normal to the sample, and the photoelectron detector is at 45° off-normal. High-energy-resolution spectra were collected using a pass-energy of 69.0 eV with a step size of 0.125 eV. For the Ag 3d_{5/2} line, these conditions produced a FWHM of 0.92 eV ± 0.05 eV. The binding energy (BE) scale is calibrated using the Cu 2p_{3/2} feature at 932.62 ± 0.05 eV and Au 4f_{7/2} at 83.96 ± 0.05 eV. Low-energy electrons at ~1 eV, 20 μA and low energy Ar⁺ ions were used to minimize sample charging during analysis.

2.5. STEM

STEM measurements were conducted with a FEI Titan 80–300 operated at 300 kV. All images were digitally recorded using a charge-coupled device camera and were analyzed using Gatan Digital Micrograph. Images were collected from at least five different locations on the grid. In general, sample preparation involved mounting of powder samples on copper grids covered with lacey carbon support films and immediate loading them into the STEM airlock to minimize exposure to atmospheric O₂. The samples were reduced at 400 °C for 1 h under 10% H₂/N₂ before measurements were taken.

2.6. Reactivity measurements

Reactivity tests for the conversion of ethanol to butadiene were conducted in a 6.35 mm outer diameter (inner diameter = 4.57 mm) fixed-bed packed bed reactor loaded with 1.0 g of catalyst. A K-type thermocouple was placed in the reactor for measurement of the catalyst bed temperature. To minimize temperature gradients, an electrical resistance heating block was installed for temperature control. Prior to testing, catalysts were first activated in situ at 450 °C for 8 h under 120

sccm of N₂. Then, the temperature was cooled to 400 °C, and the catalysts were reduced under 100 sccm of 10% H₂/N₂ for 1 h. Ethanol was fed into the system using an ISCO syringe pump and converted to gas phase using a vaporizer consisting of 6.6 mm inner diameter steel tubing filled with quartz beads. Catalyst activities were measured at 400 °C, 7 bar, and varied weight hour space velocities (WHSV) as noted. H₂ was typically used as the carrier gas. A knockout pot placed directly downstream of the reaction zone was used to collect liquid product. Gaseous effluent was analyzed online using an Inficon micro-GC (Model 3000 A) equipped with MS-5A, Plot U, alumina, and OV-1 columns and a thermal conductivity detector. Liquid samples collected from the knockout pot were analyzed separately ex situ using liquid chromatography. The ethanol conversion (single pass) and the products selectivities were calculated as presented in equations [1] and [2] below. The carbon balance was typically within 10%.

$$\text{Ethanol conversion(\%)} = \frac{100 \times (\text{moles ethanol})_{\text{in}} - (\text{moles ethanol})_{\text{out}}}{(\text{moles ethanol})_{\text{in}}} \quad (1)$$

$$\text{Carbon selectivity product}_i(\%) = \frac{100 \times \text{moles of carbon in product}_i}{\text{total carbon moles in identified products}} \quad (2)$$

2.7. Computational methods

The CP2K quantum chemical package [31] was used to compute the energetics reported at the generalized gradient approximation density functional theory (DFT) level. Geodecker-Teter-Hutter pseudopotentials describe the core region of each atom [32], and a Gaussian-plane wave hybrid basis set scheme describe the valence electrons. The Perdew–Burke–Ernzerhof exchange-correlation functional [33], Grimme's D3 dispersion correction [34], and periodic boundary conditions were used throughout. Free energies of gas phase molecules were evaluated using standard statistical mechanical methods [35], and adsorbate free energies were approximated using the entropy correlation developed by Campbell and Sellers [36]. Additive-increase/multiplicative-decrease simulations were performed in the canonical NVT ensemble using a Nosé–Hoover thermostat [37,38] in order to sample the configurational space of bound species, after which each system was annealed to < 5 K with a velocity adjustment factor of 0.9995. Although this approach does not guarantee we find the global minimum, it makes sure the final binding conformations are at least not stuck in a metastable local minimum.

We used a grand-canonical free energy minimization protocol to determine the convex hull and chemical potentials of the H* atoms adsorbed in these systems. The total (i.e., extensive) free energy cost of adding H* into the system (as compared to the gas phase chemical potential of H₂) was determined using Eq. 3.

$$\Delta G_{TOT}[N_H, \sigma] = G_{system}[N_H, \sigma] - G_{system}[N_H = 0] - \frac{N_H}{2} G_{H_2} \quad (3)$$

where N_H is the number of H atoms in the system, $G_{TOT}[N_H, \sigma]$ is the total free energy change of the system with N_H H atoms taken from the gas phase reservoir and bound to the system with a configuration denoted by σ , $E_{system}[N_H, \sigma]$ is the DFT energy of the same, and G_{H_2} is the free energy of gas phase H₂ at the partial pressure of ~7.9 bar and temperature of 400 °C used in the experiments. To find the most energetically favorable H* configuration and speciation, all binding sites were sampled before the next H atom addition. We then constructed the convex hull by connecting all ground state structures, which are themselves identified as the minimum energy configurations of N_H atoms ($N_H[\sigma]$ thus being the number of H atoms in configuration σ) that produces a monotonically increasing H* chemical potential, which was found from Eq. 4.

$$\mu_{H^*}[N_H, \sigma_i] = \frac{\Delta G_{TOT}[N_H, \sigma_i] - \Delta G_{TOT}[N_H, \sigma_{i-1}]}{N_H[\sigma_i] - N_H[\sigma_{i-1}]} \quad (4)$$

where σ_i is the H* configuration of ground state i . Once $\mu_{H^*}[N_H, \sigma_i]$ achieves a value of zero (to within the errors inherent to the adspecies entropy approximation used), the system is declared equilibrated with the gas phase.

3. Results

3.1. Pathway for n-butene production over 4%Cu/4%ZrO₂/SBA-16 and comparison with 4%Ag/4%ZrO₂/SBA-16

There are two pathways that can lead to single-bed formation of n-butene from ethanol when under H₂ environment. As shown in Fig. 1, n-butene can be produced from crotonaldehyde reduction to crotyl alcohol, followed by dehydration to 1,3-butadiene and then hydrogenation. N-butene also can be obtained from crotonaldehyde hydrogenation to butyraldehyde followed by hydrogenation to 1-butanol and then dehydration. For Ag/ZrO₂/SBA-16 catalysts, we previously demonstrated that n-butene is mainly produced from the 1,3-butadiene pathway due to effective hydrogenation of the C=O bond of crotonaldehyde [26,39]. Furthermore, replacing Ag with Cu was found to have little impact on the catalytic performance of ZrO₂/SiO₂-based catalysts for direct conversion of ethanol to butadiene [40]. This suggests that single-bed conversion of ethanol to n-butene may occur via the butadiene pathway for the 4Cu/4ZrO₂/SBA-16 catalyst. To investigate the reaction pathway over 4Cu/4ZrO₂/SBA-16, we first conducted experiments with varied space velocity.

Acetaldehyde and n-butene were the main products formed as shown in Fig. 2. In contrast with the results obtained over 4Ag/4ZrO₂/SBA-16, butadiene formation was not detected over the conversion range studied (i.e., ~30–100%). Instead, butyraldehyde and 1-butanol were formed. Their selectivities decrease from ~7% at 56% conversion to 0% at 95% conversion, indicating that they are both intermediates in the formation of n-butene. Overall, the results suggest that over 4Cu/4ZrO₂/SBA-16 n-butene is formed from the butyraldehyde pathway. This is consistent with previous results for vapor phase hydrogenation of crotonaldehyde over Cu/SiO₂ that showed preferential hydrogenation of the C=C bond of crotonaldehyde as opposed to C=O bond hydrogenation [41].

To validate the reaction pathway for n-butene production from ethanol over 4%Cu/4%ZrO₂/SBA-16, operando ¹H MAS NMR experiments were conducted. Fig. 3 depicts operando ¹H NMR spectra recorded while increasing the temperature from 42° to 210 °C. Initially, signals attributed to crotonaldehyde (9.45, 7.13, 6.18 and 2.10 ppm), ethanol (CH₂: 3.76 and CH₃: 1.24 ppm), hydrogen (4.32 ppm) and a metal-hydride species (0.16 ppm) are observed. As the temperature increases, an up-field shift indicative of ethanol vaporization is seen [42]. Peaks characteristic of diethyl ether (3.12 and 0.67 ppm also) are emerging due to ethanol dehydration. The spectra indicate that crotonaldehyde also vaporizes because gaseous peaks (9.22, 5.80, and 1.59 ppm) grow while surface adsorbed resonances disappear. Complete disappearance of crotonaldehyde signatures indicative of its conversion occurs when the temperature exceeds 186 °C. When the temperature increases from 186 °C to 210 °C butyraldehyde forms as an intermediate with characteristic peaks of the vapor phase at 9.26, 1.77, 1.2, and 0.8 ppm. A peak characteristic of surface adsorbed butyraldehyde also is visible at 9.6 ppm when temperature reaches ~210 °C. We note that the peaks attribution for butyraldehyde was confirmed by a component experiment in which the results exhibit similar chemical shifts as well as the surface adsorbed analogs (9.8, 2.5, 1.7, and 1.0 ppm) that can be seen in Fig. S1a. With further temperature elevation, butyraldehyde also is consumed, and butanol forms as a final product with characteristic peaks at 0.47, 1.08, 1.19, and 1.58 ppm. No peaks characteristic of n-butene or butadiene are seen. With the evidence provided by operando

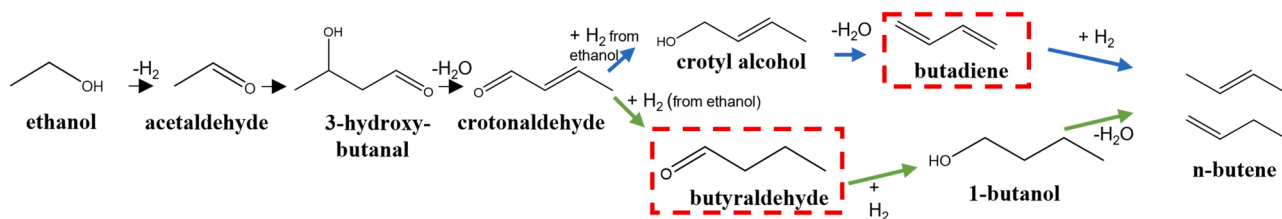


Fig. 1. Simplified reaction pathway for direct conversion of ethanol to n-butene rich olefins. Side reactions are not included.

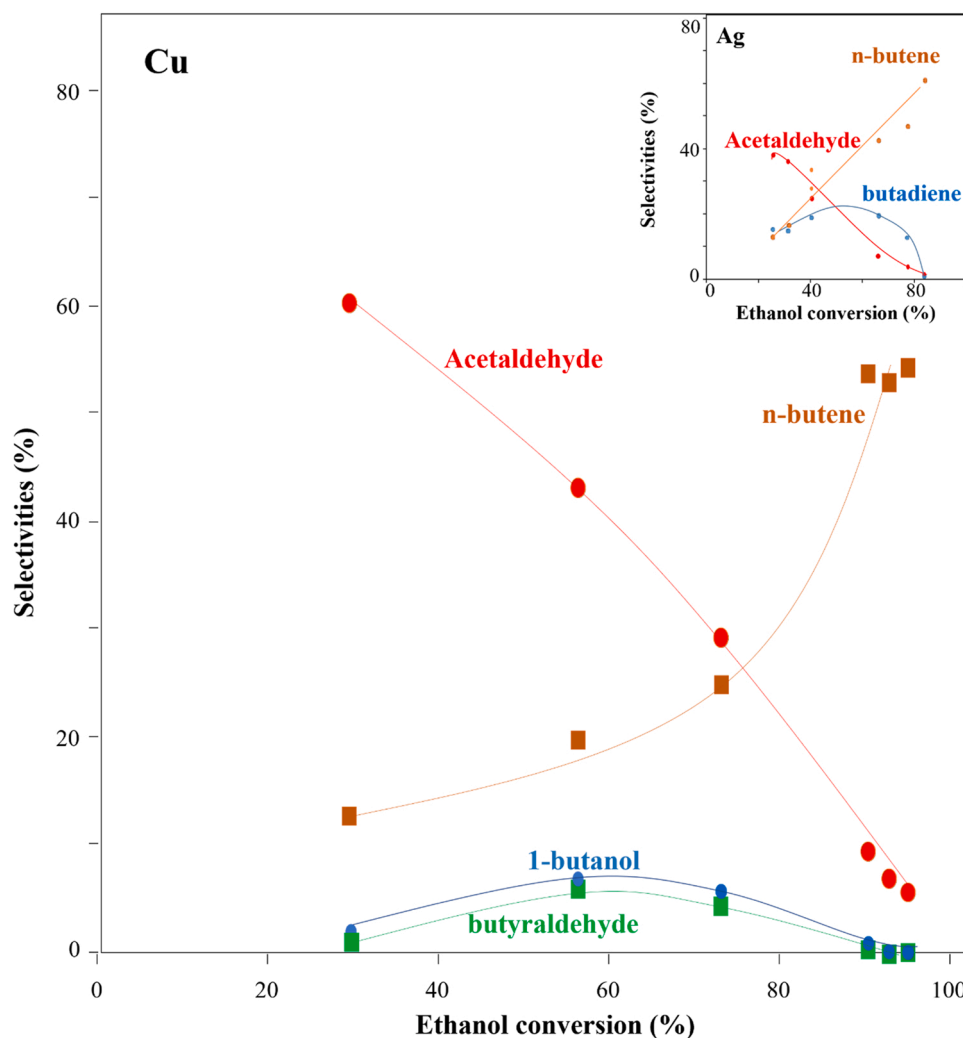


Fig. 2. Evolution of the selectivities to the main products and intermediates for direct ethanol conversion to n-butene rich olefins over 4%Cu/4%ZrO₂/SBA-16. T = 400 °C, P = 7 bar, WHSV = 0.7–53 hr⁻¹, 2 moles ethanol fed per gram catalyst, and comparison with 4%Ag/4%ZrO₂/SBA-16 (inset) from previous work [26].

¹H MAS NMR, it can be concluded unambiguously that butyraldehyde is a major intermediate during ethanol conversion to butene. On the contrary, the role of butadiene in n-butene formation seems limited.

To further understand how the nature of the metal (Cu vs. Ag) influences the reaction mechanism we conducted a computational study. DFT calculations and a grand-canonical free energy minimization protocol were used to simulate the reduction of the catalyst at the experimental temperature (400 °C) and reactant partial pressures (~7.9 bar) utilized. Here it was found how H⁺ adsorbs to the Ag or Cu nanoparticles (NP), ZrO₂, and SiO₂ sites in each of the Ag and Cu catalyst models (see Fig. S2). The H⁺ surface density increases until its binding free energy equilibrates with the gas phase (see Fig. S3 and Fig. S4). Results shown in Fig. 4 show how when at equilibrium, the Ag/ZrO₂/SiO₂ catalyst

experiences nearly 100% H⁺ spillover, with H⁺ binding primarily to the SiO₂ support and ZrO₂ as protons forming Zr(OH)₂ entirely. In contrast, the Cu/ZrO₂/SiO₂ catalyst model experiences less than 50% spillover and the Cu NP becomes saturated with H⁺ that exhibits a mildly hydridic character, inducing a decrement of ZrO₂ hydrogenation. These results show how H⁺ preferentially binds with Cu NPs but not Ag NPs when supported by ZrO₂ and SiO₂, engendering greater Lewis acidity in the Cu/ZrO₂/SiO₂ catalyst compared with the Ag/ZrO₂/SiO₂ catalyst. This greater Lewis acidity has a strong impact on the observed bifurcation point within the ethanol upgrading mechanism. The Ag catalyst presents no Zr sites that are not hydroxylated, while the Cu does. This functionality change will greatly determine which type of intermediates are produced during reaction and may help explain the improved selectivity

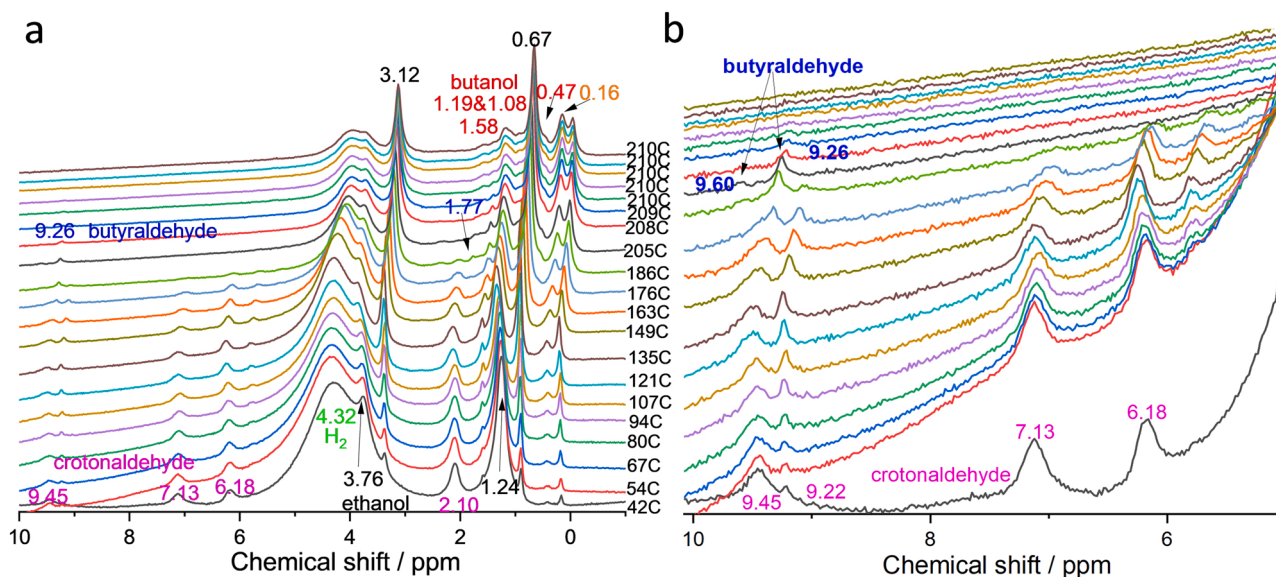


Fig. 3. ^1H NMR spectra recorded when increasing the reaction temperature from 42° to 210°C after adding a mixture of ethanol (2.2 μL) and crotonaldehyde (0.8 μL) along with 19 psig of H_2 into the in situ MAS NMR rotor. Catalyst weight = 12.5 mg.

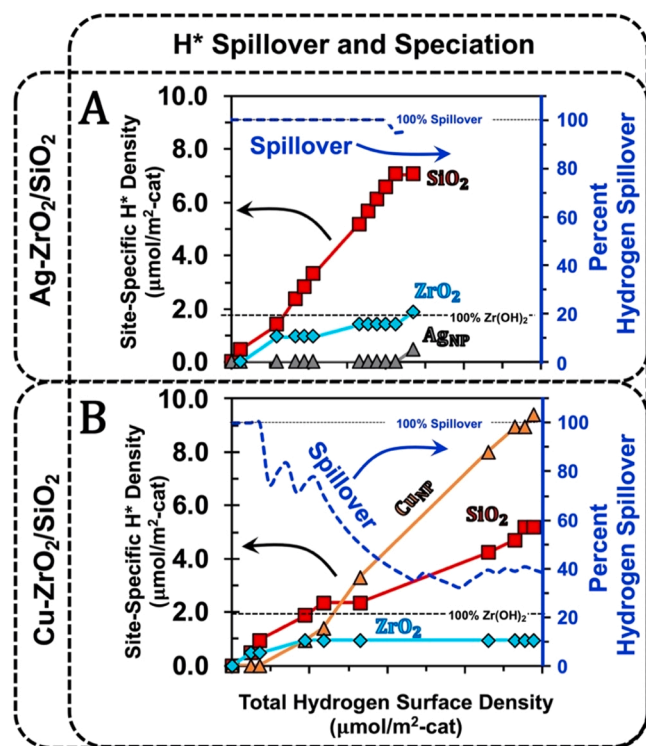


Fig. 4. Spillover of H atoms to the SiO_2 support or ZrO_2 promoter during simulated hydrogenation of (a) the $\text{Ag}/\text{ZrO}_2/\text{SiO}_2$ and (b) the $\text{Cu}/\text{ZrO}_2/\text{SiO}_2$ catalyst models, along with the H atoms which remain on the Ag or Cu nanoparticles.

toward acetaldehyde and butyraldehyde as $\text{C}=\text{C}$ bonds are preferentially attacked by the Cu catalyst instead of $\text{C}=\text{O}$ bonds.

The same models also were used to understand *how* both crotonaldehyde and ethanol prefer to bind to each catalyst. As shown in Table S1 both ethanol and crotonaldehyde bind the strongest to ZrO_2 for both catalyst systems. However, crotonaldehyde binds much stronger than ethanol (by 49 and 58 kJ/mol for the Cu and Ag catalysts, respectively), which suggests that it will outcompete ethanol for these

sites whenever formed. With the $\text{Cu}/\text{ZrO}_2/\text{SiO}_2$ catalyst ethanol binds relatively strongly to all sites. However, with the $\text{Ag}/\text{ZrO}_2/\text{SiO}_2$ catalyst ethanol binds most favorably to ZrO_2 and only weakly (or not at all) to the Ag and Ag- ZrO_2 interface sites. This suggests that the H^* available to reduce crotonaldehyde to either crotyl alcohol or butyraldehyde (see reaction pathway in Fig. 1) is vastly different between the two catalysts.

With crotonaldehyde bound to the M- ZrO_2 interface for both catalysts, we investigated the activations of its $\text{C}=\text{O}$ and $\text{C}=\text{C}$ bonds (see Fig. 5). Bader charge analysis was used to calculate the $\text{C}=\text{O}$ dipole moment of crotonaldehyde (middle panel, Fig. 5). The $\text{C}=\text{O}$ bond of crotonaldehyde is more activated with the Ag model with a dipole moment of 20.2 D compared to 16.3 D for the Cu model. This suggests that the $\text{C}=\text{O}$ bond of crotonaldehyde is more likely to be activated and reduced thereby forming crotyl alcohol with the Ag catalyst. In this scenario, crotyl alcohol maintains its $\text{C}=\text{C}$ bond and then subsequently forms butadiene upon its dehydration. Also calculated was the differential charge density, which represents how the charge is moved upon binding. With the Ag model, when crotonaldehyde is bound to the ZrO_2 sites, the oxygen of the $\text{C}=\text{O}$ bond is strongly reduced (see Fig. 5, right side). This finding corroborates the earlier finding that the $\text{C}=\text{O}$ is more likely to be activated with the Ag catalyst. In contrast, with the Cu model the $\text{C}=\text{O}$ bond shows very little change in its charge. Instead, the Cu model shows significant charge transfer to the carbon of the $\text{C}=\text{C}$ bond. Further, its $\text{C}=\text{C}$ bond preferentially binds to the Cu NP interface (see Fig. 5b). Cu's innate preference for $\text{C}=\text{C}$ bond attacks has also been shown previously [43,44]. This shows how the $\text{C}=\text{C}$ bond of crotonaldehyde preferably binds to Cu NPs thereby forming butyraldehyde. In this scenario, the $\text{C}=\text{O}$ bond of butyraldehyde remains intact until its subsequent reduction to butanol. Taken together, the preference for how crotonaldehyde binds ($\text{C}=\text{O}$ versus $\text{C}=\text{C}$) and the speciation of the relevant H^* can help rationalize the catalytic differences induced by the presence of Ag or Cu. Here we demonstrate how crotonaldehyde is more likely to be reduced to crotyl alcohol, subsequently forming butadiene over Ag catalyst or reduced to butyraldehyde over Cu catalyst. This explains *why* there exists a preferred pathway for each catalyst at the bifurcation point of the reaction pathway shown in Fig. 1.

3.2. Catalyst lifetime comparison between 4%Ag/4% ZrO_2 /SBA-16 and 4%Cu/4% ZrO_2 /SBA-16

In our prior study, under mild operating conditions (i.e., 325 °C,

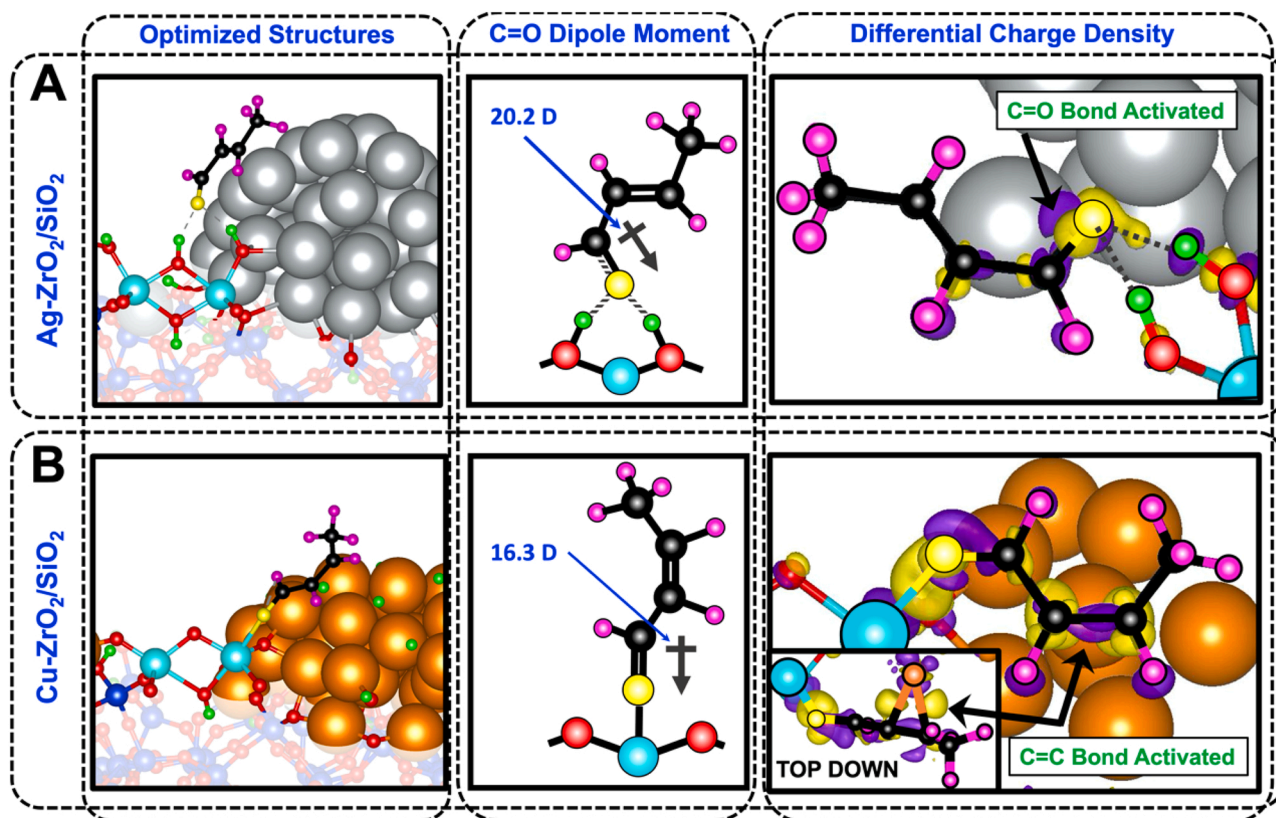


Fig. 5. Optimized structures, C=O bond dipole moments, and differential charge density plots of crotonaldehyde bound to the ZrO₂ sites of the (a) Ag/ZrO₂/SiO₂ and (b) Cu/ZrO₂/SiO₂ catalyst models. Color code for atoms: grey = Ag, orange = Cu, green = H* adspecies, turquoise = Zr, red = O, blue = Si, magenta = H atoms of crotonaldehyde, yellow = O of crotonaldehyde. The yellow and purple charge densities indicate areas where charge have been gained and lost, respectively.

WHSV = 0.23 hr⁻¹) the 4%Ag/4%ZrO₂/SBA-16 suffered from slow deactivation due mainly to coke deposition, Ag particle sintering, and partial change of oxidation state from Ag⁰ to Ag⁺ [45]. In the present work, we tested the stability of 4%Ag/4%ZrO₂/SBA-16 and 4%Cu/4%ZrO₂/SBA-16 for a period of ~100 h under severe operating conditions (i.e., high WHSV = 1.8 hr⁻¹ and high temperature of 400 °C) to accelerate any potential deactivation. As shown in Fig. 6, the 4%Ag/4%ZrO₂/SBA-16 catalyst suffers from rapid deactivation with a conversion decreasing from 88% (TOS = 19 h) to 55% (TOS = 101 h).

Butadiene formation is predominant from the start of the reaction with a selectivity equal to ~35–45% suggesting that the throughput is too fast to allow complete hydrogenation to n-butene. While the selectivity to C₃⁺ olefins (i.e., C₃–C₅ olefins) decreases with time-on-stream (TOS), the selectivity to total olefins (i.e., C₂–C₅ olefins) remains stable. This is explained by a decrease of n-butene formation accompanied by an increase in ethylene formation with TOS. The selectivity to the dehydrogenation pathway products (i.e., acetaldehyde + butadiene + n-butene + n-butane) shown in Fig. S5 decreases with TOS from ~74%

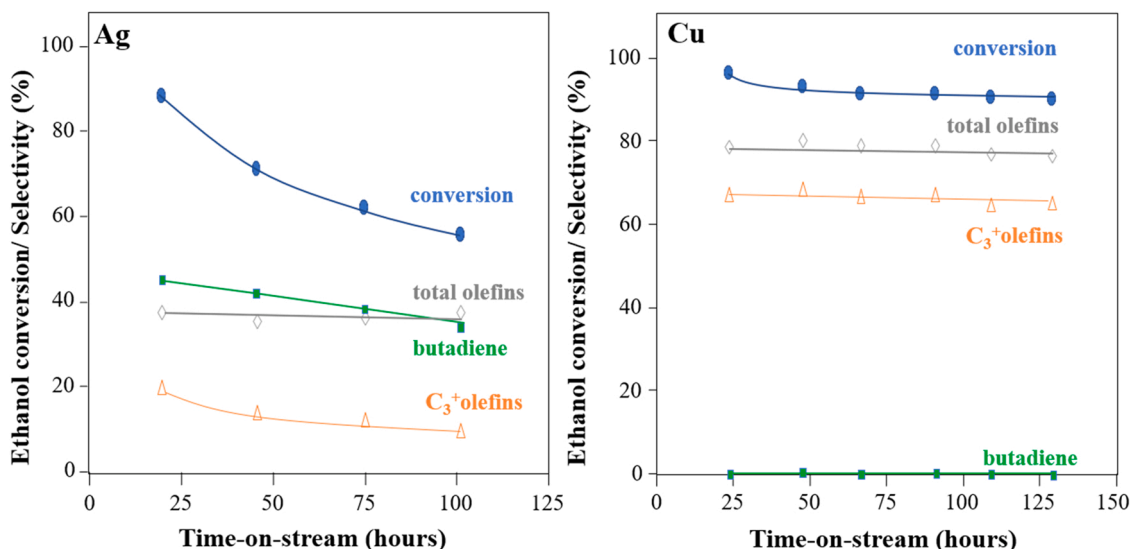


Fig. 6. Lifetime study for 4%Ag/4%ZrO₂/SBA-16 (left) and 4%Cu/4%ZrO₂/SBA-16 (right). Temperature = 400 °C, P = 7 bar, WHSV_{ethanol} = 1.8 hr⁻¹.

(TOS = 19 h) to ~50% (TOS = 101 h) meanwhile the selectivity to dehydration products (i.e., ethylene + ethane + Diethyl ether) increases from 19% to 44%. Therefore, the ethanol dehydration pathway is favored over the ethanol dehydrogenation pathway with TOS. This can be partially attributed to an increase of Ag particle size [27].

As compared to the supported Ag catalyst, the 4%Cu/4%ZrO₂/SBA-16 catalyst appears significantly more stable because the conversion decreases only slightly from 96% (TOS = 24 h) to 90% (TOS = 129 h). Additionally, the product selectivity remains stable over the 129-hour run. Contrary to the results obtained with 4%Ag/4%ZrO₂/SBA-16, the total olefin selectivity is high (i.e., ~80%), and no butadiene formation was observed. Overall, under those harsh operating conditions, the catalytic performance and stability of the 4%Cu/4%ZrO₂/SBA-16 is remarkable.

The spent Ag and Cu catalysts from the lifetime study (presented in Fig. 6) were characterized to understand the superior stability of the supported Cu catalyst. We conducted STEM analysis to investigate potential metal sintering during reactions, and representative images are shown in Fig. 7.

For 4%Ag/4%ZrO₂/SBA-16, the particle size distribution shown in Fig. 8 (left) clearly shifts toward bigger Ag particles, indicating that sintering occurs during reaction. The histograms representative of the Cu particle size distribution in Fig. 8 (right) shows that for both reduced and spent samples the majority of the particles are in the 1–2 nm size range. However, the percentage of Cu particles in this range decreases from ~55% for the reduced catalyst to ~35% for the spent sample. This is balanced by an increased number of Cu particles in the 3–5 nm range

size, indicating that Cu particles sinter during reaction. This can explain the slight decrease of conversion observed for 4%Cu/4%ZrO₂/SBA-16 in Fig. 6 (right). Furthermore, the average particle size reported in Table 1 increases by 27–30% after 100 h on stream for both catalysts indicating that the sintering rate is similar for both metals.

Thus, the higher deactivation rate for 4%Ag/4%ZrO₂/SBA-16 compared to 4%Cu/4%ZrO₂/SBA-16 cannot be solely attributed to greater sintering. Total carbon analysis results presented in Table 1 indicate that carbon deposition (i.e., coke) is about three times higher for the spent 4%Ag/4%ZrO₂/SBA-16 catalyst compared to the spent 4%Cu/4%ZrO₂/SBA-16. The larger coke deposition for the Ag catalysts leads to a plugging of the catalyst's pores as evidenced by the drastic decrease in BET surface making the active sites inaccessible and leading to faster deactivation. The high carbon deposition observed for 4%Ag/4%ZrO₂/SBA-16 is attributed to the high selectivity toward 1,3-butadiene, which indeed polymerizes quite easily. Hence, 4%Cu/4%ZrO₂/SBA-16 presents the advantage of facilitating the butyraldehyde pathway limiting deactivation due to coking as compared to 4%Ag/4%ZrO₂/SBA-16.

Given that 4%Ag/4%ZrO₂/SBA-16 catalyst deactivation is in part due to partial change of oxidation of the metal from Ag⁰ to Ag⁺ state [45], XPS was performed for the 4%Cu/4%ZrO₂/SBA-16 system. The spectra recorded for the reduced catalyst and the spent catalyst (from Fig. 6) are presented in Fig. 9.

We used the modified Auger parameter (MAP) to follow systematic changes in the final state effects without interference of surface charging. By considering the Cu 2p_{3/2} BE, the Cu L₃M₄₅M₄₅ Auger

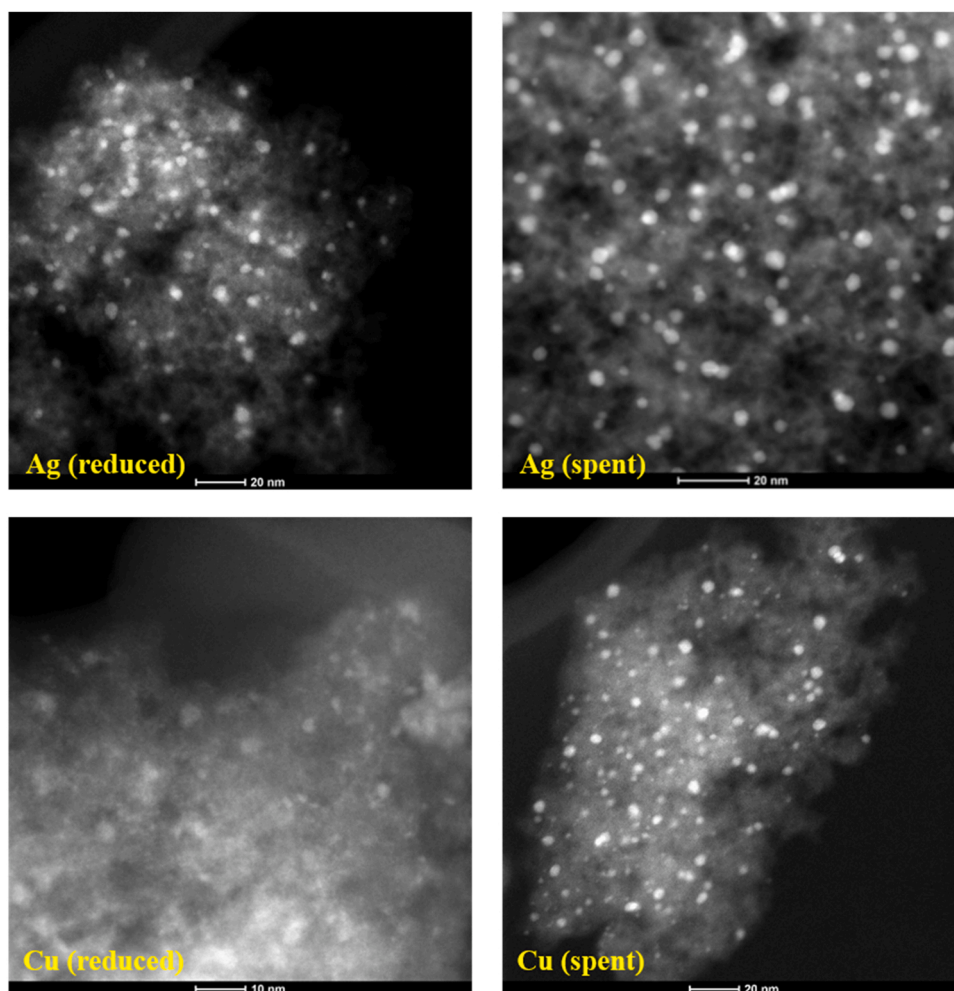


Fig. 7. STEM images for the reduced and spent 4%Ag/4%ZrO₂/SBA-16 and 4%Cu/4%ZrO₂/SBA-16. Spent catalysts from activity data presented in Fig. 4.

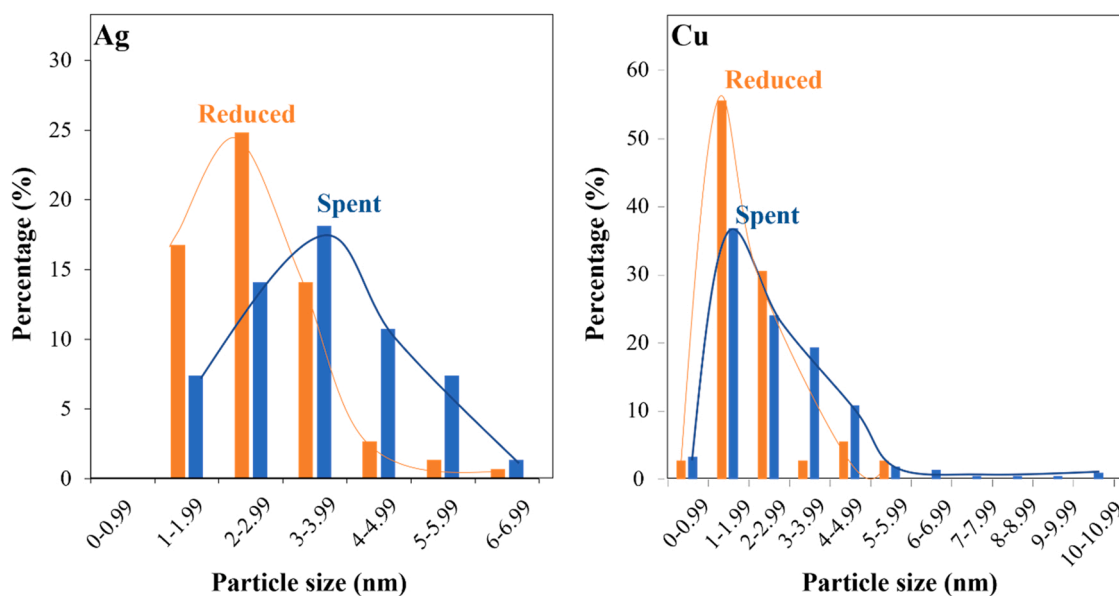


Fig. 8. Particle size distribution for the reduced and spent 4%Ag/4%ZrO₂/SBA-16 (left) and 4%Cu/4%ZrO₂/SBA-16 (right) estimated from STEM images. The spent catalysts are from activity data presented in Fig. 4.

Table 1

Carbon content, BET surface and average particle size for the fresh and spent 4% Ag/4%ZrO₂/SBA-16 and 4%Cu/4%ZrO₂/SBA-16 (from reactivity data presented in Fig. 6) and for %Cu/4%ZrO₂/dealuminated zeolite Beta (from reactivity data presented in Fig. 11).

Catalyst	Carbon content (%)	BET surface (m ² /g)	Average particle size (nm), TEM
Fresh 4%Ag/4%ZrO ₂ /SBA-16	0.03	528	2.7
Spent 4%Ag/4%ZrO ₂ /SBA-16	8.61		3.5
Fresh 4%Cu/4%ZrO ₂ /SBA-16	0.02	526	2.2
Spent 4%Cu/4%ZrO ₂ /SBA-16	2.98	497	2.8
Fresh 4%Cu/4%ZrO ₂ /Dealuminated zeolite Beta	0.02	510	10.4
Spent 4%Cu/4%ZrO ₂ /Dealuminated zeolite Beta	16.61	154	11.0

kinetic energy as well as MAP together, and the lack of Cu 2p shake-up satellite features consistent with Cu (II) typically observed at 943 eV (see Fig. S6) we are able to distinguish Cu (0) from Cu (I) and Cu (II). It has been reported that the reference MAP value (α') for Cu (0) is 1851.24 eV whereas the MAP (α') for Cu (I) is 1849.17 eV. This represents a significant difference of ~ 2.1 eV between the MAP values for Cu (0) relative to Cu (I) [46,47]. In the 4%Cu/4%ZrO₂/SBA-16 spent catalysts, the MAP value is 1851.3 eV, which is consistent within ± 0.05 eV of the MAP value of 1851.24 eV reported for Cu (0). We also know from the literature that the MAP value for Cu (II) is 1851.33 eV, and this is similar to the MAP value for Cu (0), making it difficult to separate Cu (II) from Cu (0) using the MAP [48,49]. We know from CuO reference spectra collected from Cu (II) that the Cu 2p presents observable satellite features around 943 eV (see Fig. S6). Due to the lack of characteristic Cu 2p shake-up satellite features at 943 eV for the 4%Cu/4%ZrO₂/SBA-16 catalysts, we can rule out any significant contribution from Cu (II) [50]. Hence, for the 4%Cu/4%ZrO₂/SBA-16 catalyst, Cu particles seem to remain in the metallic state during reaction. Overall, the results suggest that the lower deactivation rate observed for 4%Cu/4%ZrO₂/SBA-16 is

due to the fact that the pathway goes through a butyraldehyde intermediate as opposed to butadiene (coke precursor) intermediate limiting its deactivation as compared to 4%Ag/4%ZrO₂/SBA-16 catalyst.

3.3. Impact of the catalyst composition on the conversion and selectivity for Cu/4%ZrO₂/SBA-16 catalysts

The performance of a series of Cu/4%ZrO₂/SBA-16 catalysts with Cu loading varying between 2 and 16 wt% was tested under the same condition (i.e., $T = 400$ °C, $WHSV = 1.8$ hr⁻¹, $P = 7$ bar) to determine the impact on ethanol conversion. As previously observed for Ag/4%ZrO₂/SBA-16 catalysts [51], the results shown in Fig. 10(a) show that the increase of the Cu loading up to 8% leads to an increase of conversion.

However, a decrease in activity is observed for the highest loading (i.e., 16 wt%). This trend suggests that for Cu loading > 8%, increasing the metal loading most likely leads to an increase of Cu particles size as opposed to an increase in concentration of Cu active sites. At similar conversion of 90–96%, the product selectivity varies greatly with the Cu loading as reported in Fig. 10(b). The increase of Cu loading leads to a drastic loss of olefins and butadiene production from 89% to 71% and 5–0%, respectively. This is accompanied by a sharp increase in alkane selectivity from 3% to 17%. Thus, the increase of Cu loading increases the hydrogenation activity. While the 2%Cu/4%ZrO₂/SBA-16 catalyst presents the highest olefin selectivity (i.e., 88%) and yield (i.e., 85%), it also leads to the formation of undesired butadiene coke precursor that could lead to accelerated deactivation. Given that butadiene is only detected at the lowest Cu loading, the results suggest that the reaction may be structure sensitive. Lower Cu loading (i.e., < 4%) could favor to some extent the butene production from the crotyl alcohol/ butadiene pathway shown in Fig. 1.

Recently, we showed for ethanol upgrading over Ag/ZrO₂/SBA-16 catalysts, that switching from an inert to a reducing environment led to the formation of n-butene as opposed to butadiene. Thus, catalysts active for butadiene production could potentially be active for n-butene production under reducing conditions. In a recent study relevant to butadiene production catalysts supported on dealuminated zeolite Beta showed promising activity [52]. Hence, we investigated the impact of the support on the catalytic performance for 4%Cu/4%ZrO₂ catalysts supported on three SiO₂-based support including SBA-16, dealuminated zeolite Beta, and aluminum silicate. As reported in Table 2, the catalyst supported on SBA-16 presents the highest ethanol conversion (86%),

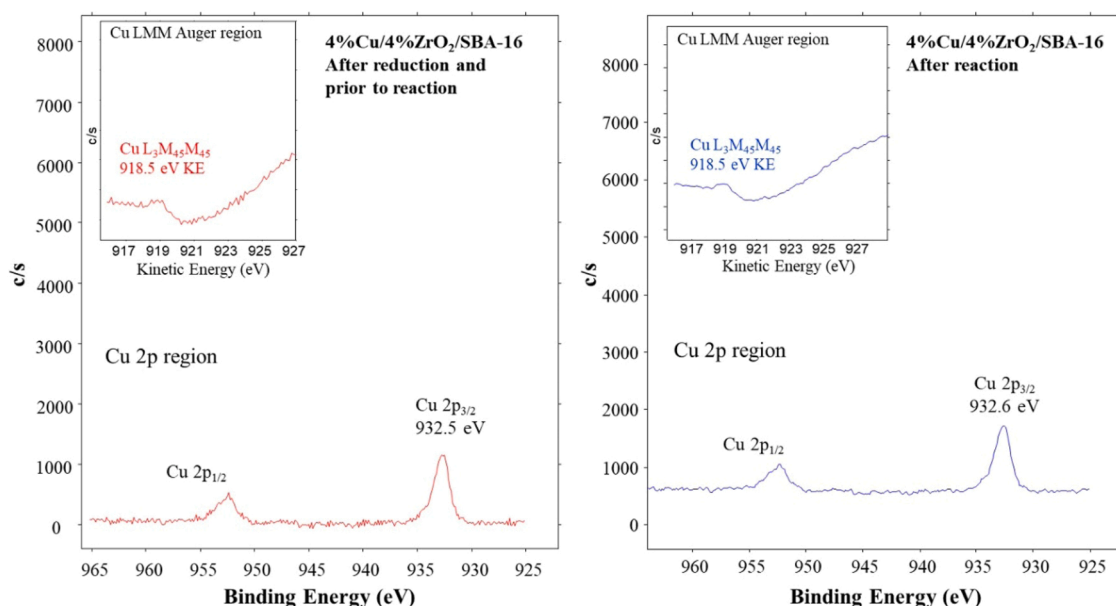


Fig. 9. XPS spectra recorded for the 4%Cu/4%ZrO₂/SBA-16 after reduction under 10%H₂/N₂ and prior to reaction (left) and for the spent 4%Cu/4%ZrO₂/SBA-16 after reaction from the results presented in Fig. 4 (right).

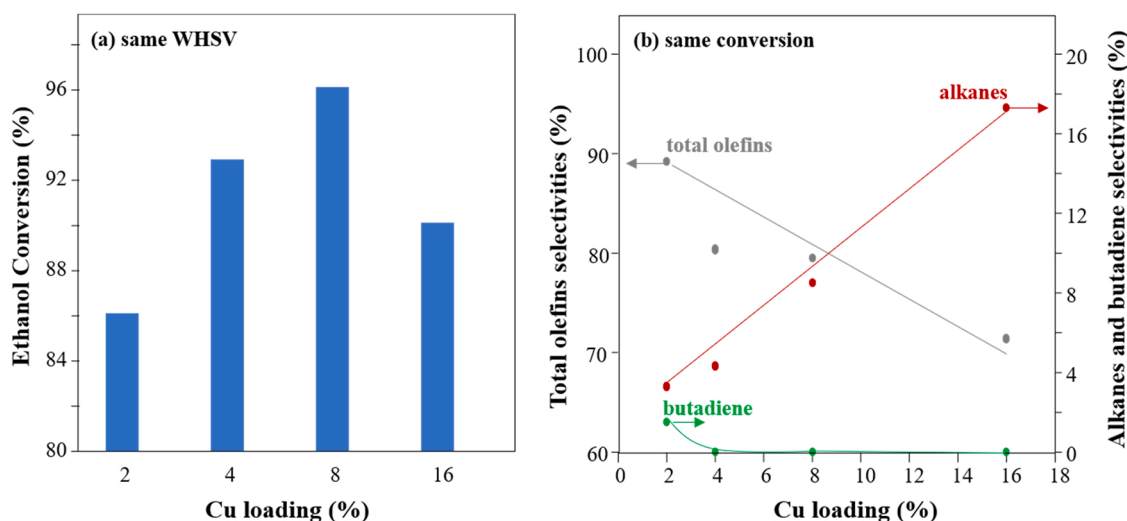


Fig. 10. Impact of the Cu loading on the conversion (left) at $\text{WHSV}_{\text{ethanol}} = 1.8 \text{ hr}^{-1}$ and on the selectivities to olefins, alkanes and butadiene (right) at similar conversion equal to 90–96%. Temperature = 400 °C, P = 7 bar.

and the one supported on dealuminated zeolite Beta presents the lowest ethanol conversion (i.e., 60.8%).

Given that selectivities can only be compared at similar conversion, the catalyst supported on dealuminated zeolite Beta was tested at lower WHSV (i.e., 0.9 hr^{-1}) at which 99.6% conversion was obtained. At a similar conversion level, the selectivity to the most desired C₃⁺ olefins is equal to 82% with the catalyst supported on SBA-16 as opposed to 62.2% with the one supported on dealuminated zeolite Beta. This is explained by an increased ethanol dehydration to ethylene and increased olefins hydrogenation to alkanes over the dealuminated zeolite Beta supported catalyst. In a previous study related to direct ethanol conversion to butene rich olefins [53], the authors claimed that Cu-Zn-Y/dealuminated Beta is more effective than Cu-Zn-Y/Silica for direct ethanol conversion to olefins with 88% and 48% olefins selectivity, respectively. However, the comparison was irrelevant because the selectivities were compared at different conversion levels (100% vs. 68%). Additionally, the silica support was a silica gel rather than a

mesoporous SBA-16 that is preferred for improving the catalytic performance of this cascade reaction [25].

The catalyst supported on SBA-16 also presents a stability advantage compared to a zeolite supported catalyst. Indeed, over 4%Cu/4%ZrO₂/dealuminated zeolite Beta, the conversion presented in Fig. 11 (a) decreases sharply from ~99% after 23 h on stream to 52% after 120 h on stream.

This is attributed to accelerated coking limiting access to the active sites. As shown in Table 1, for 4%Cu/4%ZrO₂/dealuminated zeolite Beta carbon deposit is 5.5 times higher compared to 4%Cu/4%ZrO₂/SBA-16. The rapid coking is attributed to butadiene polymerization because the butadiene selectivity shown in Fig. 11 (c) increases with TOS over 4% Cu/4%ZrO₂/dealuminated zeolite Beta while no butadiene is detected over 4%Cu/4%ZrO₂/SBA-16. Additionally, the desired olefin selectivity presented in Fig. 11(b) decreases significantly with TOS only for 4%Cu/4%ZrO₂/dealuminated zeolite Beta and is equal to 52.4% for a TOS = 120 h. This is mainly due to an increase in acetaldehyde and DEE

Table 2

Impact of the nature of the support on the catalytic performance of 4%Cu/4%ZrO₂/support. T = 400 °C, P = 7 bar, ethanol:acetaldehyde = 2:1 (wt%), TOS = 48 h.

Support	SBA-16	Aluminum Silicate	Dealuminated zeolite Beta	Dealuminated zeolite Beta
WHSV (hr ⁻¹)	1.8	1.8	1.8	0.9
Ethanol conversion (%)	86	70.4	60.8	99.6
Selectivities (%)				
Total olefins	86.7	67.5	61.3	74.8
C ₃ ⁺ olefins	82.0	67.1	54.1	62.2
Ethylene	4.7	0.4	7.2	12.6
Butadiene	0.0	0.0	20.8	0.0
Alkanes	6.2	9.6	4.8	18.2
Aromatics	0	3.9	0	1.8
Oxygenates ^a	7.1	19.0 * *	13.1	5.2

^a acetaldehyde, diethyl-ether (DEE), ethyl-acetate, butyraldehyde, 1-butanol, butanoic acid, acetone. * mainly DEE (13.3%)

selectivities both shown in Fig. 11(d). Hence, 4%Cu/4%ZrO₂/SBA-16 catalyst presents both selectivity and stability advantage compared to 4%Cu/4%ZrO₂/dealuminated zeolite Beta.

3.4. Impact of the environment (H₂/N₂ ratio) on the conversion and selectivity

Previously, for 4Ag/4ZrO₂/SBA-16 catalyst, we demonstrated that switching from a N₂ environment to an H₂ environment significantly increases the olefin selectivity from 37.8% to 80.8% because H₂ facilitates hydrogenation of butadiene, which is the main reaction intermediate. Given that the main reaction intermediate involved in the formation of n-butene is butyraldehyde as opposed to butadiene for the supported Cu catalysts, the impact of the H₂/N₂ can have on the conversion and selectivity was investigated over 2%Cu/4%ZrO₂/SBA-16 and the results are presented in Table 3. While operating under the same reaction conditions, the conversion is lower under an inert environment (i.e., 53.7%) as compared to when operating under H₂ (i.e., 95.8%). To allow selectivity comparisons under similar conversions (i.e., 53.7–60.8%), we increased the WHSV to 4.73 hr⁻¹ when operating under H₂. The total olefin selectivity decreases only from 56.4% to 52.3% when switching from an H₂ to a N₂ environment, but the C₃⁺ olefin selectivity decreases sharply from 31.6% to 9.4%. This is explained by a higher ethylene formation under N₂ (i.e., 42.9% vs. 24.8% under H₂) accompanied by a lower n-butene formation from the ethanol dehydrogenation pathway via acetaldehyde. Hence, operating under N₂ facilitates the undesired ethanol dehydration pathway and operating under H₂ environment favors the ethanol dehydrogenation pathway leading to n-butene formation.

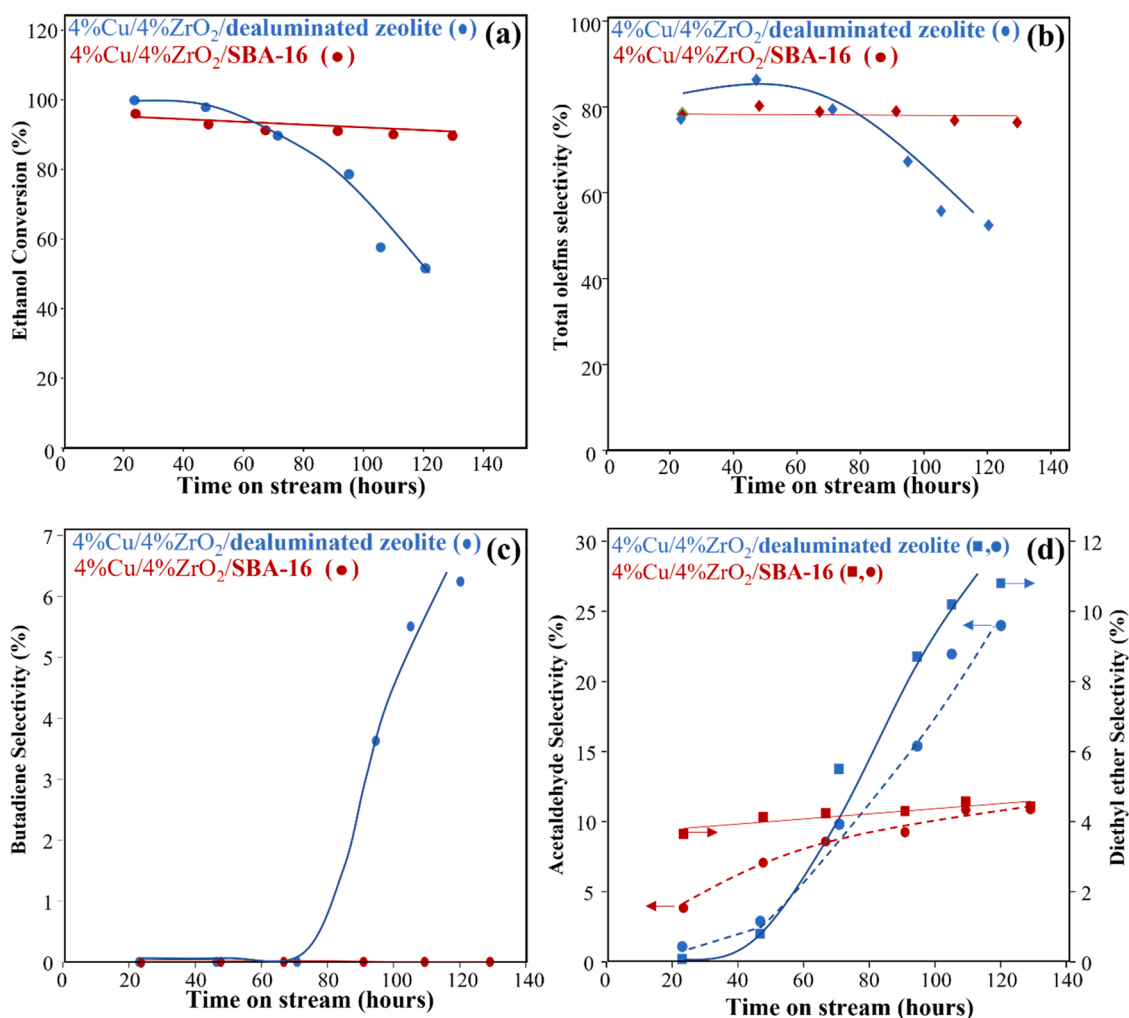


Fig. 11. Lifetime study for 4%Cu/4%ZrO₂/SBA-16 (red) and 4%Cu/4%ZrO₂/Dealuminated zeolite Beta (blue). Temperature = 400 °C, P = 7 bar, WHSV_{ethanol} = 1.8 hr⁻¹.

Table 3

Impact of the H₂/N₂ ratio on the catalytic performance of 2%Cu/4%ZrO₂/SBA-16. T = 400 °C, P = 7 bar, WHSV = 0.73 hr⁻¹.

H ₂ /N ₂ (molar)	1/0	1/1	0/1	1/0
WHSV (hr ⁻¹)	0.73	0.73	0.73	4.73
Ethanol conversion (%)	95.8	88.4	53.7	60.8
Selectivities (%) carbon based				
Total olefins	89.2	70.1	52.3	56.4
C ₃ ⁺ olefins	62.3	32.5	9.4	31.6
Ethylene	26.9	37.6	42.9	24.8
Butadiene	1.5	10.3	11.3	8.7
Alkanes	3.3	2.5	1.9	0.8
oxygenates ^a	6.0	17.1	34.5	34.1

^a mainly acetaldehyde, DEE, ethyl-acetate, butyraldehyde, 1-butanol, butanoic acid, acetone.

3.5. Impact of feedstock composition on catalytic performance

The catalytic performance of 4%Cu/4%ZrO₂/SBA-16 was tested with varied feedstocks (i.e., acetaldehyde, crotonaldehyde, or mixture of ethanol + aldehyde) and compared to the one with pure ethanol. The selected feedstocks are intermediates involved in the single-bed conversion of ethanol to n-butene. As shown in Table 4, when feeding a mixture of ethanol and acetaldehyde, the conversion and product selectivity are very similar to the ones obtained when feeding ethanol alone. The main difference is the lower ethylene selectivity (i.e., 4.7% as opposed to 12% with ethanol alone), which can be explained by the fact that the concentration of ethanol (the precursor of ethylene) in the feed is lower. With acetaldehyde feed the main products are butyraldehyde (30.7%) and ethanol (30.5%). Over ZrO₂/SiO₂ in inert atmosphere, Ordonsky et al. [54] demonstrated that acetaldehyde is converted into crotonaldehyde following the mechanism presented in Fig. 1. However, in the present study the presence of H₂ and Cu metal sites enable some acetaldehyde hydrogenation to ethanol [55]. Consequently, the crotonaldehyde intermediate produced over ZrO₂/SBA-16 acid sites reacts rapidly with the ethanol product, which leads to butyraldehyde formation via Meerwein-Ponndorf-Verley reduction. Indeed, for 4%Ag/4%ZrO₂/SBA-16 catalyst an ¹H NMR operando study demonstrated that the hydrogen from ethanol is responsible for the formation of butyraldehyde as opposed to the hydrogen from H₂ [26]. Feeding a mixture of ethanol and crotonaldehyde over 4%Cu/4%ZrO₂/SBA-16 leads to high conversion (>80%) and similar olefin selectivity (i.e., 77.6%) as the one obtained with pure ethanol feed (i.e., 80.3%). As expected, the selectivities to ethylene (2.3%) and acetaldehyde (2.1%) are lower because both ethanol dehydration to ethylene and ethanol dehydrogenation to acetaldehyde compete with crotonaldehyde reduction to 1-butanol followed by dehydration to n-butene. Overall, the results suggest that operating

Table 4

Catalytic performance of 4%Cu/4%ZrO₂/SBA-16 for conversion of ethanol, acetaldehyde, ethanol/acetaldehyde (70/30 mass ratio) and ethanol/crotonaldehyde (70/30 mass ratio). T = 400 °C, P = 7 bar, WHSV = 1.8 hr⁻¹.

Feed	ethanol	acetaldehyde	Ethanol /acetaldehyde	Ethanol /crotonaldehyde
Conversion	92.9	76.6	86/90	81/100
Total olefins	80.3	14.0	86.7	77.6
C ₃ ⁺ olefins	68.3	13.3	82.0	75.3
Ethylene	12.0	0.7	4.7	2.3
Butadiene	0	0	0	0
Alkanes	4.3	1.5	6.2	8.6
1-butanol	0.2	8.4	1.0	2.3
Acetaldehyde	7.1	-	-	2.1
butyraldehyde	0	30.7	0.4	0.7
Other oxygenates ^a	8.1	45.4 **	5.7	8.7

^a mainly, DEE, ethyl-acetate, butanoic acid, acetone. * * mainly ethanol (30.5%) and crotonaldehyde (4.4%)

with a mixture of ethanol and acetaldehyde is beneficial to the production of olefins while limiting ethanol dehydration to ethylene.

4. Conclusion

In conclusion, we report on a new Cu/ZrO₂/SBA-16 catalyst for single step conversion of ethanol to n-butene, and in comparison with our previously developed Ag/ZrO₂/SBA-16 catalyst. We demonstrated that the main reaction pathway for n-butene formation varies depending on the nature of the metal (i.e., Cu vs. Ag). While Ag promotes the formation of n-butene from a 1,3-butadiene intermediate, Cu favors a butyraldehyde intermediate pathway. Indeed, when replacing Ag with Cu, n-butene is produced mainly from the reduction of crotonaldehyde into butyraldehyde (as opposed to 1,3-butadiene) as confirmed by operando NMR experiments followed by hydrogenation into 1-butanol and dehydration into n-butene. The DFT calculations study highlighted how activation of the C=O bond of crotonaldehyde is preferred over Ag/ZrO₂/SiO₂ catalyst model, but activation of the C=C is favored over Cu/ZrO₂/SiO₂ catalyst model. Given that butadiene is a coke precursor, replacing Ag with Cu leads to a drastic increase in catalyst stability when operating under severe conditions (i.e., high temperature and high WHSV). Catalysts with Cu loadings between 2 and 16 wt% and supported on 4%ZrO₂/SBA-16 were tested and the highest olefin selectivity of 89% was achieved at 96% conversion with the 2% Cu loading. Compared to a dealuminated zeolite Beta support, the SBA-16 support clearly offers both catalytic performance and stability advantages. Indeed, butadiene formation is more predominant for the catalyst support on dealuminated zeolite Beta leading to rapid loss of conversion (i.e., 50% loss within 120 h) from coking. Conducting the reaction under H₂ as opposed to N₂ over Cu/ZrO₂/SBA-16 catalysts allows for higher conversion and selectivity to olefins as well as increased stability due to limited butadiene formation. In addition to being very effective for direct conversion of ethanol to olefins, the Cu/ZrO₂/SBA-16 catalyst system is also very active for converting mixture of ethanol + aldehydes (i.e., acetaldehyde, crotonaldehyde) to olefins. This study highlights the potential of Cu/ZrO₂/SBA-16 catalysts for production of olefins fuel precursor from ethanol with limited energy intensive ethanol dehydration to ethylene.

CRedit authorship contribution statement

Vanessa Lebarbier Dagle: Conceptualization, Methodology, Experimental investigation (catalyst synthesis and testing), Analysis, Validation, Writing – original draft, Writing – review & editing, Supervision. **Gregory Collinge:** Computational investigation, Analysis, Writing of computational section. **Mohammed Rahman:** Experimental investigation (reactivity). **Austin Winkelman:** Experimental investigation (data collection). **Wenda Hu:** Experimental investigation (NMR). **Jian Zhi Hu:** Supervision for NMR. **Libor Kovarik:** Experimental investigation (TEM). **Mark Engelhard:** Experimental investigation (XPS). **Jennifer Jocz:** Experimental investigation (catalyst synthesis). **Yong Wang:** Supervision, Writing – review & editing. **Mal-Soon Lee:** Supervision for computational investigation, Editing of the computational section. **Vassiliki-Alexandra Glezakou:** Supervision for computational investigation. **Debmalya Ray:** Computational investigation. **Roger Rousseau:** Supervision for computational investigation, Editing of the computational section. **Robert Dagle:** Conceptualization, Methodology, Writing – review & editing, Supervision.

Declaration of Competing Interest

The authors declare that they have no known competing financial interests or personal relationships that could have appeared to influence the work reported in this paper.

Data Availability

data will be made available upon request but the researchers expertise will not be shared.

Acknowledgments

The authors gratefully acknowledge funding for this research, provided by the U.S. Department of Energy (DOE), Office of Energy Efficiency and Renewable Energy, Bioenergy Technologies Office, at Pacific Northwest National Laboratory (PNNL), and in collaboration with the Chemical Catalysis for Bioenergy Consortium (ChemCatBio), a member of the Energy Materials Network. PNNL is operated for DOE by Battelle Memorial Institute. The use of catalyst characterization equipment was provided by a user proposal at the William R. Wiley Environmental Molecular Sciences Laboratory, which is a national scientific user facility sponsored by the DOE Office of Biological and Environmental Research and located at PNNL in Richland, Washington. Computational work was performed using the PNNL Research Computing facility and the National Energy Research Scientific Computing Center located at the Lawrence Berkeley National Laboratory provided by a user proposal.

The views and opinions of the authors expressed herein do not necessarily state or reflect those of the U.S. government or any agency thereof. Neither the U.S. government nor any agency thereof, nor any of their employees, makes any warranty, expressed or implied, or assumes any legal liability or responsibility for the accuracy, completeness, or usefulness of any information, apparatus, product, or process disclosed, or represents that its use would not infringe privately owned rights.

Appendix A. Supporting information

Supplementary data associated with this article can be found in the online version at [doi:10.1016/j.apcatb.2023.122707](https://doi.org/10.1016/j.apcatb.2023.122707).

References

- [1] J. Holladay, Z. Abdullah, J. Heyne, Sustainable Aviation Fuel: Review of technical pathways, DOE- EERE.
- [2] A. 2020, Airlines Fly Green.
- [3] E.S.K. Why, H.C. Ong, H.V. Lee, Y.Y. Gan, W.-H. Chen, C.T. Chong, Renewable aviation fuel by advanced hydroprocessing of biomass: challenges and perspective, *Energy Convers. Manag.* 199 (2015), 112015.
- [4] Y. Nakagawa, M. Tamura, K. Tomishige, Recent development of production technology of diesel- and jet-fuel-range hydrocarbons from inedible biomass, *Fuel Process. Technol.* 193 (2019) 404–422.
- [5] G. 2021, Four Things to Know About Sustainable Aviation Fuel (SAF).
- [6] W.-C. Wang, L. Tao, Bio-jet fuel conversion technologies, *Renew. Sustain. Energy Rev.* 53 (2016) 801–822.
- [7] H. Wei, W. Liu, X. Chen, Q. Yang, J. Li, H. Chen, Renewable bio-jet fuel production for aviation: A review, *Fuel* 254 (2019), 115599.
- [8] G. Liu, B. Yan, G. Chen, Technical review on jet fuel production, *Renew. Sustain. Energy Rev.* 25 (2013) 59–70.
- [9] P.C. Badger, Ethanol from cellulose: a general review, in: J. Janick, A. Whipkey (Eds.) *Trends in New Crops and New Uses*, ASHS Press, Alexandria, VA, 2002, pp. 17–21.
- [10] P. Roy, A. Dutta, A review of life cycle of ethanol produced from biosyn gas, *Bioeth* 1 (2013) 9–19.
- [11] H.T. Luk, C. Mondelli, D. Curulla Ferré, J.A. Steward, J. Perez-Ramirez, Status and prospects in higher alcohols synthesis from syngas, *Chem. Soc. Rev.* 46 (2017) 1358–1426.
- [12] Y. Chen, H. Zhang, H. Ma, W. Qian, F. Jin, W. Ying, Direct conversion of syngas to ethanol over Rh–Fe/γ-Al₂O₃ catalyst: promotion effect of Li, *Catal. Lett.* 148 (2018) 691–698.
- [13] H.N. Abubakar, M.C. Veiga, C. Kennes, Carbon monoxide fermentation to ethanol by *Clostridium autoethanogenum* in a bioreactor with no accumulation of acetic acid, *Bioresour. Technol.* 186 (2015) 122–127.
- [14] S. Rajagopalan, R.P. Datar, R.S. Lewis, Formation of ethanol from carbon monoxide via a new microbial catalyst, *Biomass Bioenergy* 23 (2002) 487–493.
- [15] N. Eagan, M.D. Kumbhalkar, J.S. Buchanan, J.A. Dumesic, G.W. Huber, Chemistries and processes for the conversion of ethanol into middle-distillate fuels, *Nat. Rev. Chem.* 3 (2019) 223–249.
- [16] J. Sun, Y. Wang, Recent advances in catalytic conversion of ethanol to chemicals, *ACS Catal.* 4 (2014) 1078–1090.
- [17] R.A.L. Baylon, J. Sun, K.J. Martin, P. Venkatasubramanian, Y. Wang, Beyond ketonization: selective conversion of carboxylic acids to olefins over balanced Lewis acid–base pairs, *Chem. Commun.* 52 (2016) 4975–4978.
- [18] R.D. Andrei, M.I. Popa, F. Fajula, V. Hulea, Heterogeneous oligomerization of ethylene over highly active and stable Ni–AlSBA-15 mesoporous catalysts, *J. Catal.* 323 (2015) 76–84.
- [19] M.A. Lilga, R.T. Hallen, K.O. Albrecht, A.R. Cooper, J.G. Frye, K.K. Ramasamy, Systems and processes for conversion of ethylene feedstocks to hydrocarbon fuels, Battelle Memorial Institute, United States, 2017.
- [20] J. Saavedra Lopez, R.A. Dagle, V.L. Dagle, C. Smith, K.O. Albrecht, Oligomerization of ethanol-derived propene and isobutene mixtures to transportation fuels: catalyst and process considerations, *Catal. Sci. Technol.* 9 (2019) 1117–1131.
- [21] A. Galadima, O. Muraza, Zeolite catalysts in upgrading of bioethanol to fuels range hydrocarbons: a review, *J. Ind. Eng. Chem.* 31 (2015) 1–14.
- [22] F. Ferreira Madeira, K. Ben Tayeb, L. Pinard, H. Vezin, S. Maury, N. Cadran, Ethanol transformation into hydrocarbons on ZSM-5 zeolites: influence of Si/Al ratio on catalytic performances and deactivation rate. Study of the radical species role, *Appl. Catal. A: Gen.* 443–444 (2012) 171–180.
- [23] P. Müller, S.-C. Wang, S.P. Burt, I. Hermans, Influence of metal doping on the Lewis acid catalyzed production of butadiene from ethanol studied by using modulated operando diffuse reflectance infrared Fourier transform spectroscopy and mass spectrometry, *ChemCatChem* 9 (2017) 3572–3582.
- [24] V. Blay, E. Epelde, R. Miravalles, L.A. Perea, Converting olefins to propene: ethene to propene and olefin cracking, *Catal. Rev.* 60 (2018) 278–335.
- [25] V.L. Dagle, M.D. Flake, T.L. Lemmon, J.S. Lopez, L. Kovarik, R.A. Dagle, Effect of the SiO₂ support on the catalytic performance of Ag/ZrO₂/SiO₂ catalysts for the single-bed production of butadiene from ethanol, *Appl. Catal. B: Environ.* 236 (2018) 576–587.
- [26] V.L. Dagle, A.D. Winkelman, N.R. Jaegers, J. Saavedra-Lopez, J. Hu, M. H. Engelhard, S.E. Habas, S.A. Akhade, L. Kovarik, V.-A. Glezakou, R. Rousseau, Y. Wang, R.A. Dagle, Single-step conversion of ethanol to n-butene over Ag–ZrO₂/SiO₂ catalysts, *ACS Catal.* 10 (2020) 10602–10613.
- [27] S.A. Akhade, A. Winkelman, V. Lebarbier Dagle, L. Kovarik, S.F. Yuk, M.-S. Lee, J. Zhang, A.B. Padmaperuma, R.A. Dagle, V.-A. Glezakou, Y. Wang, R. Rousseau, Influence of Ag metal dispersion on the thermal conversion of ethanol to butadiene over Ag–ZrO₂/SiO₂ catalysts, *J. Catal.* 386 (2020) 30–38.
- [28] N.R. Jaegers, M.Y. Hu, D.W. Hoyt, Y. Wang, J.Z. Hu, Development and application of in situ high-temperature, high-pressure magic angle spinning NMR, in: G. A. Webb (Ed.), *Modern Magnetic Resonance*, Springer International Publishing, Cham, 2017, pp. 1–19.
- [29] N.R. Jaegers, W. Hu, Y. Wang, J.Z. Hu, High-temperature and high-pressure in situ magic angle spinning nuclear magnetic resonance, *J. Vis. Exp.* 164 (2020), e61794.
- [30] J.Z. Hu, M.Y. Hu, Z. Zhao, S. Xu, A. Vjunov, H. Shi, D.M. Camaioni, C.H.F. Peden, J. A. Lercher, Sealed rotors for in situ high temperature high pressure MAS NMR, *Chem. Commun.* 51 (2015) 13458–13461.
- [31] J. Hutter, M. Iannuzzi, F. Schiffmann, J. VandeVondele, cp2k: atomistic simulations of condensed matter systems, *WIREs Comput. Mol. Sci.* 4 (2014) 15–25.
- [32] S. Goedecker, M. Teter, J. Hutter, Separable dual-space Gaussian pseudopotentials, *Phys. Rev. B Condens. Matter* 54 (1996) 1703–1710.
- [33] J.P. Perdew, K. Burke, M. Ernzerhof, Generalized gradient approximation made simple, *Phys. Rev. Lett.* 77 (1996) 3865–3868.
- [34] S. Grimme, J. Antony, S. Ehrlich, H. Krieg, A consistent and accurate ab initio parametrization of density functional dispersion correction (DFT-D) for the 94 elements H–Pu, *J. Chem. Phys.* 132 (2010), 154104.
- [35] D. McQuarrie, *Statistical Mechanics*, New York, New York 1975.
- [36] C.T. Campbell, J.R.V. Sellers, The entropies of adsorbed molecules, *J. Am. Chem. Soc.* 134 (2012) 18109–18115.
- [37] S. Nosé, A unified formulation of the constant temperature molecular dynamics methods, *J. Chem. Phys.* 81 (1984) 511–519.
- [38] W.G. Hoover, Canonical dynamics: equilibrium phase-space distributions, *Phys. Rev. A* 31 (1985) 1695–1697.
- [39] H. Lin, H. Qu, W. Chen, K. Xu, J. Zheng, X. Duan, H. Zhai, Y. Yuan, Promoted chemoselective crotonaldehyde hydrogenation on zirconia-doped SiO₂ supported Ag catalysts: interfacial catalysis over ternary Ag–ZrO₂–SiO₂ interfaces, *J. Catal.* 372 (2019) 19–32.
- [40] V.L. Sushkevich, I.I. Ivanova, V.V. Ordonsky, E. Taarning, Design of a metal-promoted oxide catalyst for the selective synthesis of butadiene from ethanol, *ChemSusChem* 7 (2014) 2527–2536.
- [41] E.L. Rodrigues, A.J. Marchi, C.R. Apesteguia, J.M.C. Bueno, Promoting effect of zinc on the vapor-phase hydrogenation of crotonaldehyde over copper-based catalysts, *Appl. Catal. A: Gen.* 294 (2005) 197–207.
- [42] N.R. Jaegers, Y. Wang, J.Z. Hu, Thermal perturbation of NMR properties in small polar and non-polar molecules, *Sci. Rep.* 10 (2020).
- [43] W. An, Y. Men, J. Wang, Comparative study on hydrogenation of propanal on Ni (111) and Cu(111) from density functional theory, *Appl. Surf. Sci.* 394 (2017) 333–339.
- [44] K. Yang, B. Yang, Identification of the active and selective sites over a single Pt atom-alloyed Cu catalyst for the hydrogenation of 1,3-butadiene: a combined DFT and microkinetic modeling study, *J. Phys. Chem. C* 122 (2018) 10883–10891.
- [45] F. Lin, V.L. Dagle, A.D. Winkelman, M. Engelhard, L. Kovarik, Y. Wang, Y. Wang, R. Dagle, H. Wang, Understanding the deactivation of Ag–ZrO₂/SiO₂ catalysts for the single-step conversion of ethanol to butenes, *ChemCatChem* 13 (2021) 999–1008.

- [46] L. Kover, Surface analysis by Auger and X-ray Photoelectron Spectroscopy, in: D. Briggs, J.T. Grant (Eds.), IM Publications, Chichester, 2003, pp. 421.
- [47] G. Moretti, Surface analysis by Auger and X-ray Photoelectron Spectroscopy, in: D. Briggs, J.T. Grant (Eds.), IM Publications, Chichester, 2003, pp. 501.
- [48] C.D. Wagner, Sensitivity of detection of the elements by photoelectron spectrometry, *Anal. Chem.* 44 (1972) 1050–1053.
- [49] G. Moretti, Auger parameter and Wagner plot in the characterization of chemical states by X-ray photoelectron spectroscopy: a review, *J. Electron Spectrosc. Relat. Phenom.* 95 (1998) 95–144.
- [50] R.P. Vasquez, Cu₂O by XPS, *Surf. Sci. Spectra* 5 (1998) 262.
- [51] R.A. Dagle, A.D. Winkelman, K.K. Ramasamy, V. Lebarbier Dagle, R.S. Weber, Ethanol as a renewable building block for fuels and chemicals, *Ind. Eng. Chem. Res.* 59 (2020) 4843–4853.
- [52] L. Qi, Y. Zhang, M.A. Conrad, C.K. Russell, J. Miller, A.T. Bell, Ethanol conversion to butadiene over isolated zinc and yttrium sites grafted onto dealuminated beta zeolite, *J. Am. Chem. Soc.* 142 (2020) 14674–14687.
- [53] J. Zhang, E.C. Wegener, N.R. Samad, J.W. Harris, K.A. Unocic, L.F. Allard, S. Purdy, S. Adhikari, M.J. Cordon, J.T. Miller, T.R. Krause, S. Cheng, D. Liu, M. Li, X. Jiang, Z. Wu, Z. Li, Isolated metal sites in Cu–Zn–Y/Beta for direct and selective butene-rich C₃+ olefin formation from ethanol, *ACS Catal.* 11 (2021) 9885–9897.
- [54] V.V. Ordonsky, V.L. Sushkevich, I.I. Ivanova, Study of acetaldehyde condensation chemistry over magnesia and zirconia supported on silica, *J. Mol. Catal. A: Chem.* 333 (2010) 85–93.
- [55] A.K. Agarwal, M.S. Wainwright, D.L. Trimm, N.W. Cant, Acetaldehyde hydrogenation over a Cu/SiO₂ catalyst, *J. Mol. Catal.* 45 (1988) 247–254.